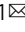


A minimal model for structure, dynamics, and tension of monolayered cell colonies

Debarati Sarkar¹, Gerhard Gompper ¹ & Jens Elgeti¹ 

The motion of cells in tissues is an ubiquitous phenomenon. In particular, in monolayered cell colonies *in vitro*, pronounced collective behavior with swirl-like motion has been observed deep within a cell colony, while at the same time, the colony remains cohesive, with not a single cell escaping at the edge. Thus, the colony displays liquid-like properties inside, in coexistence with a cell-free “vacuum” outside. We propose an active Brownian particle model with attraction, in which the interaction potential has a broad minimum to give particles enough wiggling space to be collectively in the fluid state. We demonstrate that for moderate propulsion, this model can generate the fluid-vacuum coexistence described above. In addition, the combination of the fluid nature of the colony with cohesion leads to preferred orientation of the cell polarity, pointing outward, at the edge, which in turn gives rise to a tensile stress in the colony—as observed experimentally for epithelial sheets. For stronger propulsion, collective detachment of cell clusters is predicted. Further addition of an alignment preference of cell polarity and velocity direction results in enhanced coordinated, swirl-like motion, increased tensile stress and cell-cluster detachment.

¹Theoretical Physics of Living Matter, Institute of Biological Information Processing and Institute for Advanced Simulation, Forschungszentrum Jülich, Jülich, Germany. ✉email: j.elgeti@fz-juelich.de

Many fundamental biological processes, like embryogenesis, wound healing or cancer/tumor invasion require cells to move collectively within tissues^{1–3}. The physics underlying these processes ranges from understanding actin polymerization and tread-milling for force generation^{4,5} and single cell migration^{6,7}, to the collective behavior of many migrating cells^{8–12}. Here, we focus on an observation from monolayers of migrating Madin–Darby canine kidney (MDCK) cells on surfaces, a prototypical model system for collective cell migration. Experimental observations reveal large-scale collective motion, like swirls, within the bulk of young monolayers^{13,14}, thus the display of fluid-like properties, before jamming occurs as the epithelial sheet matures^{15–18}. Interestingly, as an initial colony expands, no cells detach from the boundary—even though the bulk of the tissue remains clearly fluid-like⁹. Cohesion is strong enough that fingers of many cells can protrude at the propagating tissue front without cell detachment. Even stronger-pulling “leader cells” do not detach^{19–22}. Cells are thus in a ‘liquid-vacuum’ coexistence regime. Even more surprising, pioneering experiments have revealed that these expanding colonies are under tensile stress^{23,24}. This raises the question how this liquid-vacuum coexistence, in combination with strong collective motion and tensile stress, can be captured and understood from a minimal physical model.

An active Brownian particle (ABP) model^{25–29} for cells with standard attractive Lennard–Jones (LJ) interactions has been proposed to study cell colonies^{30,31}. However, only solid-vacuum (no fluidity of the condensed phase), or liquid-gas (finite cell density in the dilute phase) coexistence has been obtained. The coexistence of liquids with a very-low-density gas phase is of course well known in many equilibrium systems. In the biological context, for example, lipid-bilayer membranes are liquid in nature, but the critical-micelle concentration is very low, so that lipids essentially never detach from the membrane. In the modeling and simulation of lipid membranes, a similar problem of attractive interactions and fluidity exists as for cell monolayers—too strong attraction leads to solidification. In coarse-grained simulations of lipid bilayers, this problem was overcome by an interaction potential with an extended range compared with the standard Lennard–Jones potential, which provides strong adhesion while still giving enough wiggle room for the molecules that the membrane to remains the fluid phase³². In the spirit of minimal modeling, we propose an active Brownian particle (ABP) model for the cells, combined with a similar longer-range interaction potential as employed successfully for the membrane lipids. We demonstrate that the LJ potential with a wider attractive basin indeed opens up a region in phase space that displays liquid-vacuum coexistence. The size of the liquid-vacuum region expands as the basin width of LJ potential increases. The fluidity of the condensed phase implies the emergence of several interesting behaviors, like a tensile stress within the colony due to a preferred orientation of the boundary cells to the outside, as well as the detachment of cell cluster above a size threshold. When a coupling of cell polarity to the instantaneous direction of motion—which is significantly affected by the interactions with the neighboring cells—is introduced, the formation of swirls and collective cell detachment is strongly enhanced.

Results and discussion

Active Brownian particles with attraction. Liquid-vacuum coexistence requires strong inter-particle adhesion, so that cells can not detach from the main colony. Concurrently, the adhesion has to provide enough wiggling room that the cells remain locally mobile inside the condensed phase and provide fluidity to the

colony. A long-range coordinated motion of cells, like fingering or swirls, then already emerges to some extent from the self-organized motion of cells which all vary their propulsion direction independently and diffusively. However, pronounced correlations are found to require additional alignment interactions of cell orientation and direction of motions. Here, the effect of neighbors pushing (or pulling) a cell in a certain direction is assumed to induce a reaction in the cell to reorient and align its propulsion direction with its instantaneous velocity direction.

The ABP model, where each particle is a sphere (in 3D) or a disc (in 2D) which undergoes rotational Brownian motion and additionally experiences a body-fixed driving force of constant magnitude, was developed to describe active motion on the microscale^{17,33}. This model displays a rich phase behavior, most notably motility-induced phase separation^{25,26,28,34}, where persistence of motion and short-range repulsion induce cluster formation. Addition of a Lennard–Jones attraction leads to the formation of arrested clusters for small propulsion^{27,30,35}. In order to obtain liquid-like properties at strong adhesion, we follow the spirit of ref. ³² and propose an interaction potential with an extended basin of width $\bar{\sigma}$, so that

$$V_m = \begin{cases} 4\epsilon[(\sigma/r)^{12} - (\sigma/r)^6], & 0 < r \leq 2^{1/6}\sigma \\ -\epsilon, & 2^{1/6}\sigma < r \leq \tilde{r} \\ 4\epsilon[(\sigma/(r-\bar{\sigma}))^{12} - (\sigma/(r-\bar{\sigma}))^6], & \tilde{r} < r < r_{\text{cut}} \end{cases}$$

Here, σ is the particle diameter, $\tilde{r} = (2^{1/6}\sigma + \bar{\sigma})$, and ϵ is the interaction strength. This modified interaction provides a short-range repulsion or volume exclusion for the particles with separation $r < 2^{1/6}\sigma$, a force-free regime for $2^{1/6}\sigma < r \leq \tilde{r}$, and a long-range attraction for particle separation, $\tilde{r} < r < r_{\text{cut}} = 2.5\sigma$.

Our model can be interpreted from a biological perspective as follows. Cell-cell attraction is mediated by the adhesion between the rather deformable cell membranes with the attached actin cortex. While this membrane adhesion is strong (indicating large ϵ), the distance between the two cell centers can still vary over a wide range (corresponding to our $\bar{\sigma}$). Only if cells come very close to each other, the cell nuclei repel each other strongly (implying the hard-core radius σ).

For activity, each ABP is subjected to a constant active force f_0 along a body-fixed propulsion direction $\hat{\mathbf{n}}_i = (\cos \theta_i, \sin \theta_i)$. The orientation θ undergoes diffusive reorientation, and may additionally experience alignment forces. Time evolution follows a Langevin dynamics,

$$m\ddot{\mathbf{r}}_i = -\gamma\dot{\mathbf{r}}_i + \mathbf{F}_i(\mathbf{r}_i) + f_0\hat{\mathbf{n}}_i + \sqrt{2D}\boldsymbol{\eta}_i^T, \quad (1)$$

$$\dot{\theta}_i = \sqrt{2D_r}\eta_i^R.$$

Here, $\mathbf{F}_i = -\nabla_i V$ describes the interaction with other cells with the total potential V as a sum of all pair interactions, and $f_0 = v_0\gamma$ is the driving force which results in a self-propulsion velocity v_0 for an isolated cell experiencing a drag force due to substrate friction with drag coefficient γ , which is related to the thermal translational diffusion coefficient $D = k_B T/\gamma$ by the Einstein relation. Similarly, D_r is the rotational diffusion coefficient. The noise forces η are assumed to be Gaussian white-noise variables with $\langle \eta_i(t) \rangle = 0$ and $\langle \eta_i(t)\eta_j(t') \rangle = \delta_{ij}\delta(t-t')$. However, note that this is an active system, and thus both diffusion processes can in principle be independent active processes with different amplitudes, and thus do not need to satisfy the Einstein relation or fluctuation-dissipation theorem. In order to emphasize the importance of rotational over translational diffusion, we choose $D_r\sigma^2/D = 3$. The Langevin equation (with a finite particle mass) is employed to enable Verlet integration^{36,37} instead of Euler integration, which allows a much larger time step and therefore enables faster computations. m and γ are chosen such that

viscous drag dominates over inertia even at short timescales, and the dynamics of the system is in the overdamped regime.

The cohesive nature of modeled cell colonies depends on the competition between adhesion and self-propulsion. A key parameter is the potential width $\bar{\sigma}$, which controls the fluid-like consistency of the colony. Further details about model parameters can be found in the “Methods” section. In the simulation results described below, all quantities are reported in dimensionless units based on thermal energy $k_B T$, particle diameter σ , and rotational diffusion time $\tau_r = 1/D_r$. We characterize the system by three dimensionless numbers, the Péclet number, $Pe = v_0 \sigma^2 / D = 3v_0 \tau_r / \sigma$ which quantifies the activity of the system, the adhesion strength $U = \epsilon / (k_B T)$, and the potential width $\bar{\sigma} / \sigma$ which determines the wiggle room of the cells.

In order to introduce local velocity-orientation alignment, we assume alignment between propulsion direction and velocity for each cell individually^{38–40}. In our simple stochastic model, Eq. (1), the orientation dynamics in this case is determined by

$$\dot{\theta}_i = \sqrt{2D_r} \eta_i^R - k_e D_r \frac{\partial}{\partial \theta} (\mathbf{n}_i \cdot \mathbf{v}_i) \quad (2)$$

Here, k_e is the strength of particle alignment. The alignment force can be interpreted as arising from a pseudo potential $V_a = -(k_e/2)(\mathbf{v} \cdot \mathbf{n})$, acting only on the orientation \mathbf{n} , but not on \mathbf{v} . Unless noted otherwise, results concern systems without velocity-alignment interactions (i.e., $k_e = 0$).

Liquid-vacuum coexistence. We begin our analysis by exploring the available phase space spanned by activity Pe and adhesive strength U . The system is initialized with a circular cell colony with $N = 7851$ particles and a diameter 100σ (packing fraction $\phi = 0.79$) in a square simulation box of linear size 150σ . The resulting phase behavior as a function of Pe and U is displayed in Fig. 1. Here, snapshots of particle conformation after long simulation time ($t = 3300\tau_r$), together with particle mobility,

measured by the mean squared displacement

$$d_m^2 = (\mathbf{r}_i(t + t') - \mathbf{r}_i(t))^2 \quad (3)$$

averaged over several reorientation times $t' = 12\tau_r$, are employed to characterize the phases. Figure 1a shows that a line $Pe \simeq U$ separates a homogeneous gas phase at $Pe > U$ from a two-phase coexistence regime for $Pe < U$. For low activity ($Pe \ll U$), the condensed phase is solid, where particles do not show any significant movement, i.e., $d_m^2 \approx 0$. As activity increases and approaches $Pe \simeq U$, cells become mobile ($d_m^2 > 1$). A simple estimate for a pair of particles, which equates the propulsion force with the maximum of the attraction force, reveals that the detachment occurs at $Pe = 2.4U$; for larger Pe the adhesive force is no longer strong enough to keep particles together. Note that thermal fluctuations are usually rather small in this study (because $U \gg 1$). Finally, for large $Pe \gtrsim 100 \gg U$, attraction becomes negligible compared to propulsion, and the system behaves like ABPs without attractive interactions. In this case, the hard-core repulsion dominates, and cells jam due to collisions at high particle density and strong propulsion forces. This corresponds to motility-induced phase separation generally observed in repulsive ABP systems^{25,26,28,34}.

For $Pe \lesssim U$, cells are unable to detach from the colony, and the colony coexists with a cell vacuum outside. If $Pe \ll U$ and $U \gtrsim 8$, the system is clearly kinetically arrested, but as activity increases, the “wiggle room” of the potential allows particles to break the neighbor cage and move, resulting in liquid–vacuum coexistence (see Supplementary Movie 1). This state of a single cohesive colony is not induced by the initial conditions of a single circular patch, but also emerges from an initial random distribution of particles due to particle aggregation and cluster coarsening (see Supplementary Movie 2). To quantitatively characterize and clearly distinguish mobile cohesive colonies from the kinetically-arrested colonies, we employ the “mean squared particle separation” (MSPS). We choose random pairs of

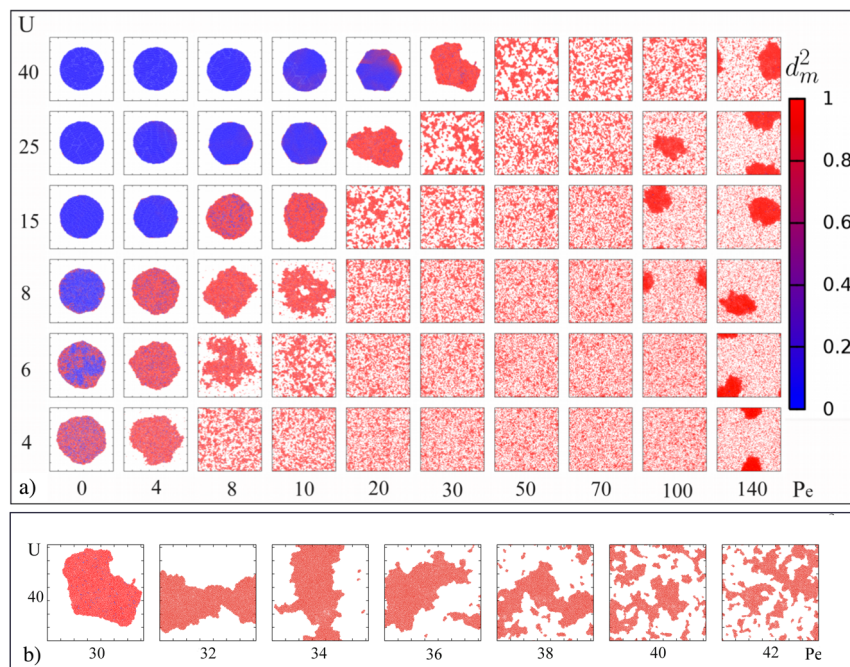


Fig. 1 Visual phase diagram. **a** Phase diagram illustrated by snapshots at the end of simulation. Here we plot the mobility profile as a function of attractive interaction U and activity Pe . We start the simulation with initial circular patch. The color code defines the magnitude of mobility. Blue means immobile and red means highly mobile colony. ($\bar{\sigma} / \sigma = 0.3$; overall packing fraction is 0.274). See Supplementary Movies 1 and 2 for the formation and dynamics of the cohesive colony at liquid vacuum coexistence for $U = 40$, $Pe = 30$. **b** Close-up of the transition region from L-V coexistence to the “many clusters” regime at $U = 40$. Above $Pe \geq 30$, the system is in the regime of a liquid colony with detached clusters, with a smooth crossover to many small clusters for $Pe \geq 36$.

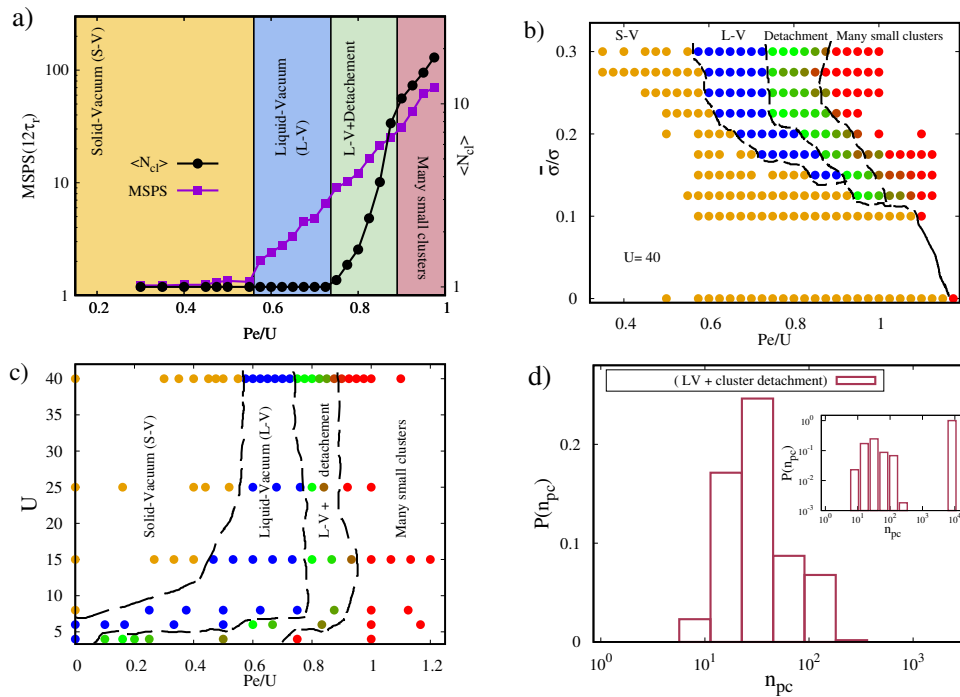


Fig. 2 Quantification of phase behavior. **a** “MSPS” (left axis) and N_{cl} (right axis) as a function of Pe/U , for fixed $U = 40$ with increasing activity. MSPS(t) is calculated at time separation $t = 12\tau_p$. The orange area indicates S–V coexistence, the blue area L–V coexistence, the green area L–V coexistence with small detached cell clusters in the gas phase, and the red area a homogeneous phase of many small clusters. Results are for $\bar{\sigma}/\sigma = 0.3$. **b** Phase diagram as a function of the potential width $\bar{\sigma}$ for fixed $U = 40$. Note that the potential width $\bar{\sigma}$ needs to be sufficiently large, with $\bar{\sigma}/\sigma \geq 0.15$, to allow liquid-vacuum coexistence. **c** Phase diagram various U as a function of rescaled Péclet number, Pe/U , for fixed $\bar{\sigma}/\sigma = 0.3$. **d** Cluster-size distribution of detached clusters, of size n_{pc} at $\bar{\sigma}/\sigma = 0.3$, $U = 40$, and $Pe = 32$. Inset: Same data in log-log representations, which also includes the parent colony along with the detached clusters.

cells m and n inside the colony at time t_p , which are initially at contact with a center-center distance less than 1.1σ , and measure the squared separation of this pair over time. We average over N_p such pairs at different initial times t_p :

$$MSPS(t) = \frac{1}{N_p} \sum_{N_p} (\mathbf{r}_m(t_p + t) - \mathbf{r}_n(t_p + t))^2. \quad (4)$$

A characteristic feature of the arrested dynamics in a solid phase is that particles do not exchange neighbors, so that the MSPS plateaus at $MSPS < (1.2\sigma)^2$. In a fluid phase, particles exchange neighbors at a constant rate, and MSPS increases linearly with time (see also Supplementary Note 1 and Supplementary Fig. 2). Thus the MSPS is good indicator of fluid-like behavior. Here, we choose $MSPS > (1.2\sigma)^2$ at time $t = 12\tau_p$ as a definition of fluid-like behavior. To quantify cohesiveness, we turn to a cluster analysis, where particles are identified to be in the same cluster if their distance is less than the cutoff distance r_{cut} . The condensed phase-vacuum coexistence is then signaled by cluster number $N_{cl} = 1$. Figure 2a displays MSPS ($t = 12\tau_p$) and N_{cl} as a function of Pe/U . For $Pe \lesssim 0.55U$, the system remains cohesive and solid. As activity increases, MSPS increases as well, but the colony remains cohesive, clearly identifying the liquid-vacuum (L–V) coexistence region. Further increasing activity ($Pe \gtrsim 0.75U$) leads to the occasional detachment of small clusters (above a threshold size) from the parent colony (see discussion below). Interestingly, occasional cluster detachment is not sufficient to disintegrate the parent colony, as detached clusters can rejoin the parent colony, which thereby coexists with a gas of small clusters. Increasing activity further leads to an increasingly fractal structure of the main cluster, and a more homogeneous density distribution of the whole system with many irregular clusters (see Fig. 1b). We define somewhat arbitrarily the

transition to the “many-small clusters” regime, when the average number of clusters exceeds a threshold, $N_{cl} \geq 10$.

Figure 2b, c display different cuts through the phase space, to elucidate the region of stability of different regimes. The results in Fig. 2b show that a minimum width $\bar{\sigma}/\sigma \simeq 0.15$ of the potential well is necessary to observe a liquid-vacuum coexisting phase. Thus, the width $\bar{\sigma}/\sigma$ plays a crucial role to achieve a cell colony with fluid-like dynamics at strong adhesion. The importance of Pe/U as the relevant variable to distinguish two-phase coexistence from a one-phase gas-like region, is emphasized by Fig. 2c, which demonstrates that the boundaries between the different regimes occur at $Pe/U \simeq 0.55, 0.75$, and 0.875 , for $U \gtrsim 20$. Note that all these boundaries appear at Pe/U values, which are much smaller than the unbinding threshold $Pe/U \simeq 2.4$ of particle pairs.

For Péclet numbers $Pe \gtrsim 0.75U$, small clusters are able to detach from the parent colony. This process can be characterized by the cluster-size distribution $P(n_{pc})$, see Fig. 2d. The peak of the distribution for clusters in the size range from 10 to 100 indicates that particles escape collectively. We do not observe the escape of any single cell from the colony in this regime. This can be understood from a simple argument, which considers a small semi-circular patch of n_{pc} particles at the boundary of the colony (see Supplementary Notes 2–3 and Supplementary Figs. 3–4). The patch has an interface with the colony of length proportional to $\sqrt{n_{pc}}$. If all particle orientations point in roughly the same direction (outwards), then the patch can unbind when $n_{pc} > n_{pc}^* \simeq 12.7(U/Pe)^2$, i.e., for sufficiently large patch size, a size which decreases rapidly with increasing Pe . The probability for all particles in such a cluster to be roughly aligned depends on the Péclet number, as particles move toward the boundary with preferred outward orientation⁴¹. However, the particle mobility in the fluid phase is very small due to the dense packing of neighbors, so that the characteristic ballistic

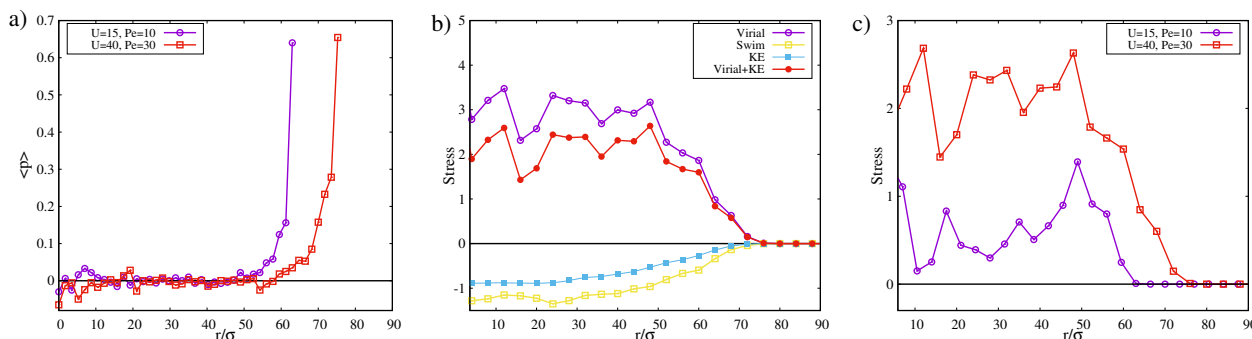


Fig. 3 Stress profile. **a** Averaged polarization vector of the circular patch for $\bar{\sigma} = 0.3\sigma$ at $L-V$ coexisting state for two different activity. **b** Different components of the stress profile at $\bar{\sigma} = 0.3\sigma$ and $U = 40$, $Pe = 30$. “Virial” stress arising from cell-cell interactions (purple line), “active” stress due to propulsion, also called swim-stress (yellow line), “kinetic” (ideal gas) stress (light-blue line), and the total stress (virial + kinetic, red line) **c** The total stress profile for different adhesive strength in $L-V$ coexisting states at $U = 15, 40$. The stress is generated in the boundary region of the colony; outside of the colony, the stress vanishes.

motion of ABPs for times less than τ_r is completely suppressed (see Supplementary Fig. 1). Therefore, polar ordering is mainly seen at the edge of the colony, see Fig. 3a. Cluster formation therefore arises mainly from the increased mobility of pre-aligned particles at the boundary (see Supplementary Movie 3).

Stress profile-tensile colonies. To gain a better understanding of the properties of the liquid-like cohesive colony, we analyze the polarization field of the active force and the stress profile. Figure 3a shows that the averaged local polarization is zero inside the colony, but points outwards at the boundary. This is in contrast to what is typically found for motility-induced clustering^{25,28,42–44}. The reason is that the attractive interactions keep outward-oriented particles at the boundary of the colony—which would otherwise move away—combined with the fluidity of the colony which allows local particle sorting near the boundary, similar to the behavior of isolated self-propelled particles in confinement^{41,45}. This mechanism is rationalized with a simple dumbbell of two ABPs as described in Supplementary Note 5.

The alignment of motility forces at the boundary should lead to an increase of tensile stress. Note that we refer to the stress within the cell layer; due to force balance, this stress is of course balanced by an opposite and equal stress in the substrate. Indeed, in experiments the deformation of the substrate is used to measure the net forces on the cell layer. Via integration of these substrate forces, the stress in the cell layer is then obtained. This procedure results in equivalent stress profiles in our simulations (see Supplementary Notes 4 and Supplementary Fig. 5). For the liquid colonies in coexistence with the vacuum phase, we find significant tensile stress in the center (see Fig. 3c). Because cells near the boundary on average pull outwards, the tension builds up near the boundary, and remains constant inside the colony where cells are randomly oriented. The total stress in the colony has two contributions: the interaction (virial) and the kinetic contribution. In addition, we consider the swim stress⁴⁴. In a dense liquid, at liquid-vacuum coexistence, the inter-particle contributions dominantes, whereas the swim stress is comparatively small (Fig. 3b). Figure 4 shows the dependence of the total (virial+kinetic) central stress in the colony on the activity. In the solid regime, the central stress is negative due to the passive surface tension, resulting in a Laplace pressure proportional to U . Increasing activity leads to more liquid-like consistency, facilitating enhanced outward particle orientation at the edge, and hence tensile stress. Interestingly, the stress is found to be a linearly increasing function of Pe over the whole investigated range, $0 < Pe \leq 30$, i.e., both in the solid and liquid regime of the colony. This indicates that the enhanced particle sorting occurs

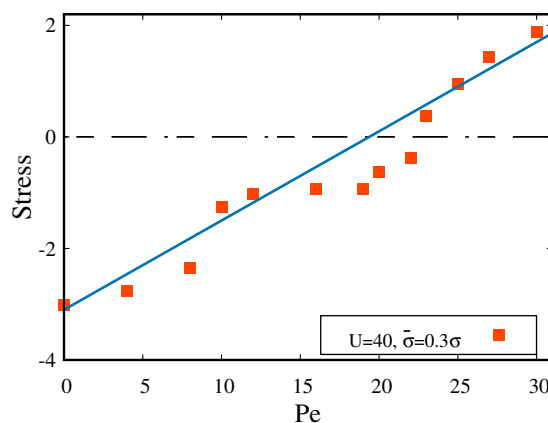


Fig. 4 Activity increases tension. Total central stress calculated in the area starting from the center to a radius 30σ as a function of activity, Pe , for $U = 40$ and $\bar{\sigma} = 0.3\sigma$. The transition from S-V to L-V coexistence occurs at $Pe = 23$ (compare Fig. 2c), which essentially coincides with Peclet number where central stress changes sign.

mainly near the edge, and an increased edge mobility exists already in the solid phase near the S-L phase boundary. A tensile stress in cell colonies has been observed similarly in experiments, where the average stress within a spreading cell sheet increases as a function of distance from the leading edge³³. We also simulated a quasi-one-dimensional (rectangular channel) geometry and obtained the total stress in the colony by integration of the net substrate forces, as in experiments. Consistently, it increases from zero outside to a finite tensile stress in the center (see Supplementary Note 4 and Supplementary Fig. 5).

Coordinated motion-motion alignment. In experimental observations, long-range velocity correlations are often visible in the bulk of spreading epithelial sheets^{13,14}. ABPs with adhesion display significant velocity correlations even without explicit alignment interactions (see Supplementary Fig. 7, and refs. 17,46). However, as ABPs display independent orientational diffusion, it is evident that realistic long-range correlations require some type of velocity alignment. We employ a local velocity-orientation alignment mechanism, in which cell propulsion direction (=cell polarity) relaxes toward the instantaneous cell velocity, resulting from the forces induced by its neighbors^{38–40}, as introduced in Eq. (2). Without alignment, correlations arise from a small group of cells pointing in the same direction by chance, and thus

moving collectively more easily and furthermore dragging other cells along. The alignment interaction stabilizes and enhances this effect. In presence of velocity alignment, the velocity field shows

an enhanced coordinated motion with prominent swirls in the bulk of the colony and fingering at the edge (see Fig. 5a).

We quantify the spatial correlations by the velocity–velocity correlation function

$$C_{vv}(r) = \left\langle \frac{\sum_i \delta \mathbf{v}(\mathbf{r}_i) \cdot \delta \mathbf{v}(\mathbf{r}_i + \mathbf{r})}{\sum_i \delta \mathbf{v}(\mathbf{r}_i) \cdot \delta \mathbf{v}(\mathbf{r}_i)} \right\rangle, \quad (5)$$

as a function of distance r , where the brackets denote an average over all directions and time. Here, velocities are measured relative to the average velocity $\bar{\mathbf{v}}$, of the whole colony, i.e., $\delta \mathbf{v}(\mathbf{r}) = \mathbf{v}(\mathbf{r}) - \bar{\mathbf{v}}$, to avoid finite-size effects. The correlations decay exponentially with a characteristic length scale, ξ_{vv} (see Supplementary Note 6 and Supplementary Fig. 8). Figure 5b displays the correlation length ξ_{vv} as a function of alignment strength k_e for various adhesive interactions. For fixed adhesion and activity, increasing alignment strength k_e facilitates a transition from the solid to the liquid state of the colony. Furthermore, the alignment coupling leads to stronger correlations, as indicated by the monotonic increase of ξ_{vv} with $k_e v_0$, and thus to swirls and fingers. Eventually, fingering is so strong that clusters detach, and the colony is no longer cohesive (see Supplementary Movie 5). Close to the transition, detached clusters are even larger than without alignment (see Fig. 5c). Indeed, in the case shown in Fig. 5c, the smallest observed cluster contains 16 particles.

Nevertheless, correlation lengths up to $\xi_{vv} = 10\sigma$ can be achieved in a cohesive colony, quite comparable to the 5 to 10 times cell size obtainable in experiments^{13,17}. Also, the tensile stress at the colony center increases (see inset of Fig. 5b) and becomes positive at sufficiently large $k_e v_0$. The critical alignment strength $k_e v_0$, where the colony is liquefied and the tensile stress becomes positive, increases with attraction strength U .

Conclusions and outlook. We have presented a minimal model for the fluidization of cell colonies, which consists of active Brownian particles with adhesion. An attractive potential with increased basin width yields non-equilibrium structures, phase behavior and dynamics, which capture relevant features of biological cell colonies. The main observation is that for sufficient basin width $\bar{\sigma}$, moderate adhesion, and propulsion, the system exhibits liquid-vacuum coexistence, i.e., all particles agglomerate into a single colony displaying liquid-like properties, while the outside remains devoid of any particles. This is reminiscent of in vitro experiments of MDCK colonies, where cells show strong motion, while remaining perfectly cohesive, even when forced to migrate in long narrow strips with strong tension buildup⁴⁷. Furthermore, the fluidity of the colony in our model results in outward ordering of particle orientations at the edge, thus leading to tension in the colony. This is consistent with the results of traction force microscopy, which show that MDCK colonies are typically under tension²³. Our model demonstrates that no alignment interaction or growth mechanism need to be evoked to explain such tensile forces—the motility of the cells combined with liquid properties of the colony suffice. As motility force increases, particles start to detach from the parent colony, however not as single cells but collectively in small clusters of cells.

A quantitative comparison of our results with those of in-vitro experiments requires of course to take into account many additional contributions, like the formation of an actin cable at the leading edge^{46,48}. Interestingly, these models also employed a wide attractive basin—however without exploring its role.

Finally, we have demonstrated how velocity–polarity alignment can further enhance fluidity, tension, and fingering of the colony, and collective cell detachment. Indeed, with velocity–polarity alignment, simulations look very reminiscent of real MDCK

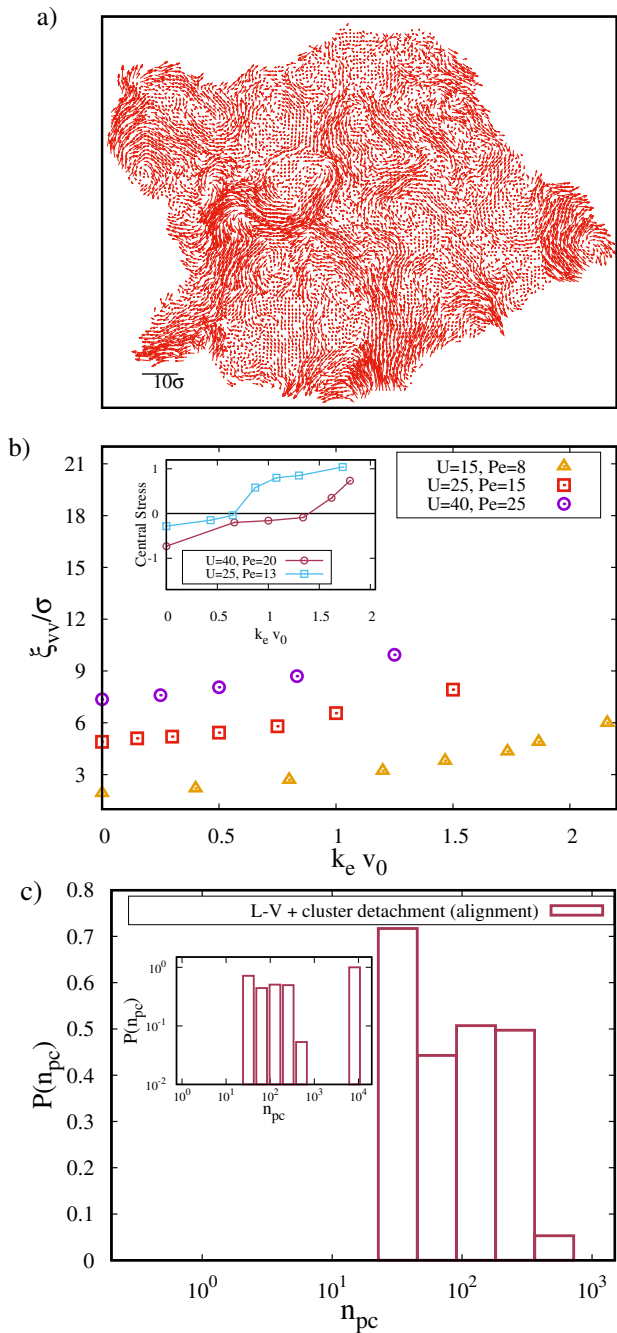


Fig. 5 Dynamics of a cell colony with orientation-velocity alignment interactions. **a** Velocity fluctuation field of the full cell colony for $U = 40$, $Pe = 25$, and $k_e v_0 = 1.25$ at $\bar{\sigma} = 0.3\sigma$, which displays prominent swirls in the bulk and finger-like structures at the edge. See also Supplementary Fig. 7, and Movies 4 and 5. **b** Characteristic correlation length ξ_{vv} , extracted from velocity correlation, as a function of alignment strength k_e , for different attractive interactions U and activities Pe , as indicated, with $\bar{\sigma} = 0.3\sigma$. The colony is in the fluid state for $k_e v_0 = 0$. Inset: Variation of total central stress as a function of alignment strength k_e , for adhesive strength $U = 25, 40$ ($\bar{\sigma} = 0.3\sigma$). For both data sets, the colony is in the solid state for $k_e = 0$, and transits to a liquid state at $k_e v_0 \approx 0.65$ and $k_e v_0 \approx 1.3$ for $U = 25$ and $U = 40$, respectively. **c** Cluster size distribution with velocity alignment ($U = 40$, $Pe = 28$, $\bar{\sigma}/\sigma = 0.3$, and $k_e v_0 = 1.4$, thus in the “Liquid-Vacuum + Detachment” regime).

colonies, displaying strong fingering at the edge, high tension and long-ranged velocity correlations.

Our model also provides a tentative explanation for another biological phenomenon. When metastatic cells detach from a tumor, they typically detach collectively, as small groups of five cells or large aggregates^{49–51}, into the stroma and migrate to reach blood or lymph vessels. At the edge of the liquid-vapor region of our model, particles show exactly this type of behavior; the colony is no longer perfectly cohesive, but clusters of cells begin to detach.

In the future, we will look into mixtures of motile and immotile cells—and also in three dimensions, where it was shown that the motile cells sort to the periphery⁵².

An interesting next question is how these results will be affected by cell growth. Of course, if growth is slow, the dynamics will be independent of growth and the phenomenology will be unchanged. However, when time scales of growth and motion become comparable, novel phenomena may arise.

Methods

Implementation and simulation parameters. For numerical implementation of our model, we use the LAMMPS molecular simulation package⁵³, with in-house modifications to describe the angle potential and the propulsion forces, as described above. The system consists of $N = 7851$ particles (cells) in a 2D square simulation box of size $L_x = L_y = 150\sigma$ with periodic boundary conditions, unless noted otherwise. With velocity-orientation-alignment interaction, the simulation is carried out in a box of size $L_x = L_y = 250\sigma$. For the extended LJ interaction potential, we use the cut-off distance $r_{\text{cut}} = 2.5\sigma$. For numerical efficiency, we chose a finite mass $m = 1$ and drag coefficient $\gamma = 100$ such that the velocity relaxation time m/γ is much smaller than all physical time scales. The equations of motion are integrated with a velocity Verlet algorithm, with time step $\Delta t = 0.001$. Each simulation is run for at least 11×10^7 time steps, with rotational diffusion coefficient $D_r = 0.03$ this corresponds to a total simulation time longer than $3000\tau_r$, where τ_r is the rotational decorrelation time.

Polarization vector. We define the spatial-temporal average polarization p for the quasi-circular cell colony by the projection of the orientation vector $\hat{\mathbf{n}}$ of the particle on the radial direction from the center of mass of the colony, i.e.,

$$\langle p(r', t) \rangle = \frac{1}{N} \sum_{i=1}^N (\hat{\mathbf{n}}_i \cdot \hat{\mathbf{r}}'_i) \delta(r' - |\mathbf{r}'_i|) / \sum_{i=1}^N \delta(r' - |\mathbf{r}'_i|) \quad (6)$$

where $\mathbf{r}'_i = \mathbf{r}_i - \mathbf{r}_{\text{cm}}$, and \mathbf{r}_{cm} is the center-of-mass position at a particular time t . Here, $\delta(r)$ is a smeared-out δ -function of width σ . $\langle p \rangle$ is further averaged over time.

Stress calculation. The stress in numerical simulations of particle-based systems with short-range interactions in thermal equilibrium consists of two contributions: The virial stress and the kinematic stress. The virial contribution is

$$\Delta V \Sigma_{\alpha\alpha}^{\text{virial}} = -\frac{1}{2} \sum_{i=1}^N \sum_{j=1}^N \langle \lambda_{ij} \mathbf{r}_{ij} \cdot \mathbf{F}_{ij} \rangle, \quad (7)$$

where \mathbf{F}_{ij} represents the pair-wise interaction between particle i and j and $\mathbf{r}_{ij} = \mathbf{r}_i - \mathbf{r}_j$. λ_{ij} denotes the fraction of the line connecting particle i and j inside of the volume ΔV . Here $\Sigma_{\alpha\alpha}$ are the diagonal stress-tensor components, without Einstein convention. The kinetic contribution is given by

$$\Delta V \Sigma_{\alpha\alpha}^{\text{kinetic}} = -\sum_{i=1}^N m \langle \dot{\mathbf{r}}_i^2 \Lambda_i \rangle \quad (8)$$

where $\dot{\mathbf{r}}_i$ denotes the velocity of particle i , and $\Lambda_i(\mathbf{r})$ is unity when particle i is within ΔV and zero otherwise.

For non-equilibrium ABP systems, additional terms have been suggested. In ABP systems with short-range repulsion, it has been shown that the pressure is a state function, depending only on activity, particle density, and interaction potential, but *not* on the interaction with confining walls^{44,54–56}. In comparison to passive systems, activity implies a new contribution to pressure, which is called the swim pressure. The calculation of the local stress in an ABP system is a matter of an ongoing debate, which mainly concerns the form of the active term. We follow ref. 44, and define a swim stress by

$$\Delta V \Sigma_{\alpha\alpha}^{\text{swim}} = -\frac{\gamma}{\gamma_R} \sum_{i=1}^N \langle v_{0i} \mathbf{n}_i \cdot \dot{\mathbf{r}}_i \Lambda_i \rangle \quad (9)$$

where γ_R is the damping factor which is related to the rotational diffusion coefficient as $\gamma_R = 2D_r$. Notably, in the dense fluid state in coexistence with vacuum

we are focusing on in this work, the active-stress component is much smaller than the expected free particle swim stress. This is in line with results for the pressure contributions in repulsive ABP systems at coexistence between a high-density and a low-density phase, where the swim pressure in the high-density phase is negligible⁴⁴.

In experiments, the stress is accessible via the traction forces exerted by the cells on the substrate. The stress is then obtained from force balance $\partial_x \Sigma_{xx} = -f_x^{\text{traction}}$. We identify the traction forces of our cells as $f^{\text{traction}} = f_a \mathbf{n} - \gamma \mathbf{v}$, i.e., we assume that cells exert their active propulsion force $f_a \mathbf{n}$ on the substrate, and experience friction forces $-\gamma \mathbf{v}$ which also arise from interaction with the substrate.

Supplementary Fig. 5 shows that these integrated traction forces agree very well with $\Sigma = \Sigma^{\text{virial}} + \Sigma^{\text{kinetic}}$. We thus define the stress as $\Sigma = \Sigma^{\text{virial}} + \Sigma^{\text{kinetic}}$.

Data availability

The data that support the findings of this study are available from the corresponding authors upon reasonable request.

Code availability

For numerical implementation of our model, we use the LAMMPS molecular simulation package⁵³, with in-house modifications to describe the angle potential and the propulsion forces, as described above. The small code modifications used for this study are available from the corresponding authors upon reasonable request.

Received: 31 July 2020; Accepted: 8 December 2020;

Published online: 26 February 2021

References

- Martin, P. & Parkhurst, S. M. Parallels between tissue repair and embryo morphogenesis. *Development* **131**, 3021 (2004).
- Friedl, P., Hegerfeldt, Y. & Tusch, M. Collective cell migration in morphogenesis and cancer. *Int. J. Dev. Biol.* **48**, 441 (2004).
- Lecaudey, V. & Gilmour, D. Organizing moving groups during morphogenesis. *Curr. Opin. Cell. Biol.* **18**, 102 (2006).
- Burridge, K. & Chrzanowska-Wodnicka, M. Focal adhesions, contractility, and signaling. *Annu. Rev. Cell Dev. Biol.* **12**, 463 (1996).
- Giannone, G. et al. Lamellipodial actin mechanically links myosin activity with adhesion-site formation. *Cell* **128**, 561 (2007).
- Lauffenburger, D. A. & Horwitz, A. F. Cell migration: review a physically integrated molecular process. *Cell* **84**, 359 (1996).
- Keren, K. et al. Mechanism of shape determination in motile cells. *Nature* **453**, 475 (2008).
- Matsubayashi, Y., Ebisuya, M., Honjoh, S. & Nishida, E. Erk activation propagates in epithelial cell sheets and regulates their migration during wound healing. *Curr. Biol.* **14**, 731 (2004).
- Puliafito, A. et al. Collective and single cell behavior in epithelial contact inhibition. *Proc. Natl Acad. Sci. USA* **109**, 739 (2012).
- Bindschadler, M. & McGrath, J. L. Sheet migration by wounded monolayers as an emergent property of single-cell dynamics. *J. Cell Sci.* **120**, 876 (2007).
- Serra-Picamal, X. et al. Mechanical waves during tissue expansion. *Nat. Phys.* **8**, 628 (2012).
- Trepat, X. & Sahai, E. Mesoscale physical principles of collective cell organization. *Nat. Phys.* **14**, 671 (2018).
- Angelini, T. E. et al. Cell migration driven by cooperative substrate deformation patterns. *Phys. Rev. Lett* **104**, 168104 (2010a).
- Angelini, T. E. et al. Glass-like dynamics of collective cell migration. *Proc. Natl Acad. Sci. USA* **108**, 4714 (2011).
- Bi, D., Lopez, J. H., Schwarz, J. M. & Manning, M. L. A density-independent rigidity transition in biological tissues. *Nat. Phys.* **11**, 1074 (2015).
- Bi, D., Yang, X., Marchetti, M. C. & Manning, M. L. Motility-driven glass and jamming transitions in biological tissues. *Phys. Rev. X* **6**, 021011 (2016).
- Garcia, S. et al. Physics of active jamming during collective cellular motion in a monolayer. *Proc. Natl Acad. Sci. USA* **112**, 15314 (2015).
- Krajnc, M., Dasgupta, S., Zihler, P. & Prost, J. Fluidization of epithelial sheets by active cell rearrangements. *Phys. Rev. E* **98**, 022409 (2018).
- Omelchenko, T., Vasiliev, J. M., Gelfand, I. M., Feder, H. H. & Bonder, E. M. Rho-dependent formation of epithelial “leader” cells during wound healing. *Proc. Natl Acad. Sci. USA* **100**, 10788 (2003).
- Poujade, M. et al. Collective migration of an epithelial monolayer in response to a model wound. *Proc. Natl Acad. Sci. USA* **104**, 15988 (2007).
- Angelini, T. E. et al. Velocity fields in a collectively migrating epithelium. *Biophys. J.* **98**, 1790 (2010b).

22. Vishwakarma, M. et al. Mechanical interactions among followers determine the emergence of leaders in migrating epithelial cell collectives. *Nat. Commun.* **9**, 3469 (2018).
23. Trepap, X. et al. Physical forces during collective cell migration. *Nat. Phys.* **5**, 426 (2009).
24. Reffay, M. et al. Interplay of RhoA and mechanical forces in collective cell migration driven by leader cells. *Nat. Cell Biol.* **16**, 217 (2014).
25. Fily, Y. & Marchetti, M. C. Athermal phase separation of self-propelled particles with no alignment. *Phys. Rev. Lett.* **108**, 235702 (2012).
26. Redner, G. S., Hagan, M. F. & Baskaran, A. Structure and dynamics of a phase-separating active colloidal fluid. *Phys. Rev. Lett.* **110**, 055701 (2013a).
27. Redner, G. S., Hagan, M. F. & Baskaran, A. Reentrant phase behavior in active colloids with attraction. *Phys. Rev. E* **88**, 012305 (2013b).
28. Wysocki, A., Winkler, R. G. & Gompper, G. Cooperative motion of active Brownian spheres in three-dimensional dense suspensions. *Eur. Phys. Lett.* **105**, 48004 (2014).
29. Elgeti, J., Winkler, R. G. & Gompper, G. Physics of microswimmers—single particle motion and collective behavior: a review. *Rep. Prog. Phys.* **78**, 056601 (2015).
30. Navarro, R. M. & Fielding, S. M. Clustering and phase behaviour of attractive active particles with hydrodynamics. *Soft Matter* **11**, 7525 (2015).
31. Prymidis, V., Paliwal, S., Dijkstra, M. & Filion, L. Vapour-liquid coexistence of an active Lennard-Jones fluid. *J. Chem. Phys.* **145**, 124904 (2016).
32. Cooke, I. R., Kremer, K. & Deserno, M. Tunable generic model for fluid bilayer membranes. *Phys. Rev. E* **72**, 011506 (2005).
33. Smeets, B. et al. Emergent structures and dynamics of cell colonies by contact inhibition of locomotion. *Proc. Natl Acad. Sci. USA* **113**, 14621 (2016).
34. Buttinoni, I. et al. Dynamical clustering and phase separation in suspensions of self-propelled colloidal particles. *Phys. Rev. Lett.* **110**, 238301 (2013).
35. Moggetti, B. M. et al. Living clusters and crystals from low-density suspensions of active colloids. *Phys. Rev. Lett.* **111**, 245702 (2013).
36. Tuckerman, M., Berne, B. J. & Martyna, G. J. Reversible multiple time scale molecular dynamics. *J. Chem. Phys.* **97**, 1990–2001 (1992).
37. Isele-Holder, R. E., Jäger, J., Saggiorato, G., Elgeti, J. & Gompper, G. Dynamics of self-propelled filaments pushing a load. *Soft Matter* **12**, 8495 (2016).
38. Szabó, B. et al. Phase transition in the collective migration of tissue cells: experiment and model. *Phys. Rev. E* **74**, 061908 (2006).
39. Basan, M., Elgeti, J., Hannezo, E., Rappel, W. J. & Levine, H. Alignment of cellular motility forces with tissue flow as a mechanism for efficient wound healing. *Proc. Natl Acad. Sci. USA* **110**, 2452 (2013).
40. Lam, K. N. T., Schindler, M. & Dauchot, O. Self-propelled hard disks: implicit alignment and transition to collective motion. *New J. Phys.* **17**, 113056 (2015).
41. Elgeti, J. & Gompper, G. Wall accumulation of self-propelled spheres. *Eur. Phys. Lett.* **101**, 48003 (2013).
42. Fily, Y., Henkes, S. & Marchetti, M. C. Freezing and phase separation of self-propelled disks. *Soft Matter* **10**, 2132–2140 (2014).
43. Digregorio, P. et al. Full phase diagram of active brownian disks: from melting to motility-induced phase separation. *Phys. Rev. Lett.* **121**, 098003 (2018).
44. Das, S., Gompper, G. & Winkler, R. G. Local stress and pressure in an inhomogeneous system of spherical active Brownian particles. *Sci. Rep.* **9**, 6608 (2019).
45. Fily, Y., Baskaran, A. & Hagan, M. F. Dynamics of self-propelled particles under strong confinement. *Soft Matter* **10**, 5609 (2014).
46. Sepúlveda, N. et al. Collective cell motion in an epithelial sheet can be quantitatively described by a stochastic interacting particle model. *PLoS Comput. Biol.* **9**, e1002944 (2013).
47. Vedula, S. R. K. et al. Emerging modes of collective cell migration induced by geometrical constraints. *Proc. Natl Acad. Sci. USA* **109**, 12974–12979 (2012).
48. Tarle, V. et al. Modeling collective cell migration in geometric confinement. *Phys. Biol.* **14**, 035001 (2017).
49. Friedl, P. & Gilmour, D. Collective cell migration in morphogenesis, regeneration and cancer. *Nat. Rev. Mol. Cell Biol.* **10**, 445 (2009).
50. Christiansen, J. J. & Rajasekaran, A. K. Reassessing epithelial to mesenchymal transition as a prerequisite for carcinoma invasion and metastasis. *Cancer Res.* **66**, 8319 (2006).
51. Clark, A. G. & Vignjevic, D. M. Modes of cancer cell invasion and the role of the microenvironment. *Curr. Opin. Cell Biol.* **36**, 13 (2015).
52. Palamidessi, A. et al. Unjamming overcomes kinetic and proliferation arrest in terminally differentiated cells and promotes collective motility of carcinoma. *Nat. Mater.* **18**, 1252–1263 (2019).
53. Plimpton, S. Fast parallel algorithms for short-range molecular dynamics. *J. Comput. Phys.* **117**, 1–19 (1995).
54. Takatori, S. C., Yan, W. & Brady, J. F. Swim pressure: stress generation in active matter. *Phys. Rev. Lett.* **113**, 028103 (2014).
55. Solon, A. P. et al. Pressure is not a state function for generic active fluids. *Nat. Phys.* **11**, 673–678 (2015).
56. Speck, T. & Jack, R. L. Ideal bulk pressure of active Brownian particles. *Phys. Rev. E* **93**, 062605 (2016).

Acknowledgements

Financial support by the Deutsche Forschungsgemeinschaft (DFG) through the priority program SPP1726 “Microswimmers—from single particle motion to collective behavior” is gratefully acknowledged. Simulations were performed with computing resources granted by RWTH Aachen University under project RWTH0475. We thank Roland G. Winkler (Jülich) for many helpful discussions concerning active stress.

Author contributions

G.G. and J.E. designed research, D.S. performed simulations and analyzed data, all authors discussed results and wrote the manuscript.

Funding

Open Access funding enabled and organized by Projekt DEAL.

Competing interests

The authors declare no competing interests.

Additional information

Supplementary information The online version contains supplementary material available at <https://doi.org/10.1038/s42005-020-00515-x>.

Correspondence and requests for materials should be addressed to J.E.

Reprints and permission information is available at <http://www.nature.com/reprints>

Publisher's note Springer Nature remains neutral with regard to jurisdictional claims in published maps and institutional affiliations.



Open Access This article is licensed under a Creative Commons Attribution 4.0 International License, which permits use, sharing, adaptation, distribution and reproduction in any medium or format, as long as you give appropriate credit to the original author(s) and the source, provide a link to the Creative Commons license, and indicate if changes were made. The images or other third party material in this article are included in the article's Creative Commons license, unless indicated otherwise in a credit line to the material. If material is not included in the article's Creative Commons license and your intended use is not permitted by statutory regulation or exceeds the permitted use, you will need to obtain permission directly from the copyright holder. To view a copy of this license, visit <http://creativecommons.org/licenses/by/4.0/>.

© The Author(s) 2021